Advanced Materials Interfaces

ADVANCED MATERIALS INTERFACES Open Access

www.advmatinterfaces.de

RESEARCH ARTICLE OPEN ACCESS

Sensitive and Spatially-Resolved Electrochemiluminescence via Micropatterning

Yuliang Shao[1] | Tatiana Starikova[1] | Mengzhen Xi[2] | Maria Vittoria Balli[2] | Emanuele Luigi Sciuto[3] | Gabriele Giagu[2] | Vincenzo Paratore[3] | Carmelo Corsaro[4] | Enza Fazio[4] | Sabrina Conoci[3] | Luca Prodi[2,5] | Giovanni Valenti[2] | Pavel A. Levkin[1,6]

[1]Karlsruhe Institute of Technology (KIT), Institute of Biological and Chemical Systems – Functional Molecular Systems (IBCS-FMS), Karlsruhe, Germany | [2]Department of Chemistry "Giacomo Ciamician" Alma Mater Studiorum – University of Bologna Via Gobetti 85, Bologna, Italy | [3]Department ChiBioFarAm, University of Messina, Messina, Italy | [4]Department of Mathematics, Informatics, Physical and Hearth Sciences – MIFT University of Messina, Messina, Italy | [5]IRCCS Azienda Ospedaliero-Universitaria di Bologna, Bologna, Italy | [6]Karlsruhe Institute of Technology (KIT), Institute of Organic Chemistry (IOC), Karlsruhe, Germany

Correspondence: Giovanni Valenti (g.valenti@unibo.it) | Pavel A. Levkin (pavel.levkin@kit.edu)

Received: 20 April 2026 | **Revised:** 19 May 2026 | **Accepted:** 21 May 2026

Keywords: diagnostics | electrochemiluminescence | micropatterning | multiplexing | photochemistry

ABSTRACT

Electrochemiluminescence (ECL) biosensing offers high sensitivity and low background but remains limited by the lack of simple strategies for electrode patterning, signal confinement, and multiplexed detection. Here, we report a silica nanoparticle–based coating and photopatterning approach for gold electrodes that enables spatially resolved and multiplexed ECL detection. The resulting electrode architecture confines aqueous droplets to designated locations and supports localized ECL signal generation. Compared with bare gold electrodes, the modified surfaces exhibit up to a ten-fold increase in ECL intensity, which correlates with reduced charge-transfer resistance and improved electron-transfer kinetics. The patterned electrodes are compatible with magnetic bead–based immunoassays and allow parallel ECL measurements from multiple spatially separated regions on a single chip. Multiplexed detection is demonstrated using the synthetic SARS-CoV-2 spike protein as a model analyte. This coating and patterning strategy provides a straightforward route to spatially resolved ECL electrodes and can be applied to multiplexed electrochemical and bioanalytical measurements where signal confinement and multiplexing are required.

1 | Introduction

Infectious diseases caused by bacterial and viral pathogens continue to threaten human health, global economies, and social stability [1, 2]. The recent COVID-19 pandemic underscored how delays in pathogen identification can accelerate outbreaks, overwhelm healthcare systems, and result in enormous economic and human loss [3, 4]. Thus, rapid and accurate detection of pathogens is essential for both clinical diagnostics and public health surveillance.

Over the past decades, molecular and immunological methods have been established as clinical gold standards. Polymerase chain reaction (PCR) amplifies DNA sequences through thermal cycling [5] and its derivatives, including quantitative PCR (qPCR) for real-time quantification and reverse-transcription PCR (RT-PCR) for RNA analysis [6–9], provide outstanding sensitivity and specificity [10–13] but require complex equipment and centralized laboratories [14, 15]. Isothermal amplification methods such as loop-mediated isothermal amplification (LAMP) [16] and recombinase polymerase amplification (RPA) [17] simplify nucleic acid

detection, yet remain prone to nonspecific amplification and limited multiplexing [18]. On the other hand, immunoassays – including enzyme-linked immunosorbent assays (ELISA) [19] and lateral flow assays (LFAs) [20, 21] – offer simplicity and low cost but suffer from reduced sensitivity, cross-reactivity, and poor scalability [22, 23]. Emerging technologies such as next-generation sequencing (NGS) enable unbiased identification of known and novel pathogens but remain costly and complex, while mass spectrometry approaches such as MALDI-TOF improve bacterial identification yet require prior culture and are less sensitive when it comes to viral detection [24–27].

These limitations have spurred growing interest in biosensor-based technologies for rapid and portable diagnostics. Electrochemical biosensors offer miniaturization, low cost, and high sensitivity, while optical methods such as fluorescence and surface plasmon resonance (SPR) provide versatile signal readout formats [28, 29]. Among these, electrochemiluminescence (ECL) biosensing has emerged as a particularly promising technology. ECL is an analytical technique in which electrochemically generated species at electrode surfaces undergo electron-transfer reactions, producing luminescent excited states. Since the signal generation is tightly controlled by the electrochemical potential, which provides temporal and spatial resolution as well as the possibility of using simpler optical instrumentation, reduced background and interferences are obtained [30–32]. Recent progress in ECL has moved beyond the conventional $Ru(bpy)_3^{2+}$/TPrA system and has substantially broadened both the chemical toolbox and the application scope of the technique. New emitter designs, including activatable molecular dyes [33], quantum dots [34], carbon nitrides [35], and organic/organometallic luminophores [36, 37], have enabled tunable emission, improved efficiency, and expanded compatibility with aqueous bioanalytical systems [38]. In parallel, advances in co-reactant chemistry have revealed that the distance, lifetime, and reactivity of radical intermediates strongly influence ECL efficiency, particularly in bead-based and surface-confined assays [39, 40]. Mechanistic studies using ECL imaging, time-dependent ECL, and trap-state engineering have further clarified how near-electrode radical generation, charge-transfer kinetics, and excited-state formation determine signal output [41, 42]. These developments have enabled new applications ranging from ultrasensitive immunoassays and cell imaging to electrocatalytic reaction mapping and local chemical-environment sensing [43, 44]. Within this rapidly developing field, spatially resolved and multiplexed ECL platforms remain particularly attractive because they combine the intrinsic low background of ECL with miniaturized, parallelized assay formats. Beyond luminophore design, assay configuration and electrode materials play a critical role in performance. The sandwich immunoassay format is the most widely employed strategy in ECL biosensing, in which a capture antibody immobilized on the electrode binds the target pathogen and a secondary antibody labeled with an ECL luminophore completes the "sandwich," providing high specificity and signal amplification [45]. This configuration is particularly attractive if the immunoassay is immobilized on a magnetic microbead (MMB) where for a simple magnetic field the analyte can be separated by the biological matrix and concentrated in the proximity of the electrode. ECL has been applied to detect biomolecules (proteins, microRNAs, DNA), small molecules, metal ions, pathogens, and even more complex targets such as cells or protein aggregates in clinical, environmental, and food safety fields [46].

To meet the demand for detecting multiple analytes simultaneously, several multiplexing strategies have been investigated. One common approach is potential-resolved multiplexing, in which different ECL luminophores with distinct onset potentials are used, enabling simultaneous detection of multiple targets by applying varied potentials in a single system [47]. A second strategy is spatially resolved multiplexing, where multiple electrode regions are patterned on a chip and functionalized with different probes, allowing each detection channel to generate an independent ECL signal at the same potential [45, 48]. Spectrum-resolved multiplexing has also been investigated, where luminophores with different emission wavelengths (e.g., $Ru(bpy)_3^{2+}$, quantum dots) are employed, and signals are distinguished optically by their spectral profiles [49, 50]. Despite progress, these strategies often involve complex electrode modifications, signal cross-talk, or limited scalability, leaving room for improvement.

Here, we report a silica nanoparticle–based coating for gold electrodes that combines spatially resolved multiplexing with magnetic microbead–based sandwich immunoassays. The coating is applied by spray deposition and further functionalized by thiol-ene photochemistry, producing uniform, spatially confined hydrophilic regions separated by superhydrophobic background enabling droplet and, thus, sample confinement. This approach offers four key advantages (Figure 1): (i) creation of multiplexed detection channels on a single chip through a simple and low-cost electrode modification, (ii) compatibility with magnetic microbead–based capture assays, (iii) up to 10-fold enhancement of the ECL signal compared with the original gold electrodes, and (iv) reusability for repeated measurements with limited performance loss. Together, this platform provides a practical route toward next-generation ECL biosensors, with the potential to advance clinically relevant multiplexed diagnostics for rapid pathogen detection and broader public health applications.

2 | Results and Discussion

2.1 | Fabrication, Application, and Partial Removal of Functionalized Silica Coating

To enable patterned ECL detection, colloidal solution of vinyl-functionalized silica nanoparticles was prepared as a spray-coating precursor by reacting commercial fumed silica with vinyltrimethoxysilane (VTMS) in ethanol under sonication in acidic solution. Dynamic light scattering (DLS) showed a hydrodynamic diameter of 196 ± 15 nm for nanoparticle agglomerates in solution (Figure S1). Upon spray-coating on gold electrodes, the particles form a uniform porous overlayer that serves as a tunable scaffold for subsequent surface functionalization and photopatterning (Figure 2).

As illustrated in Figure 2, the prepared vinyl-functionalized silica nanoparticles were spray-coated onto the gold electrode, and the coated chips were annealed at 150°C for 1 h. After forming the porous nanoparticle film, the coating was hydrophobized by applying a 1H,1H,2H,2H-perfluorodecanethiol (PFDT) solution and exposing the surface to mild UV irradiation (UVA

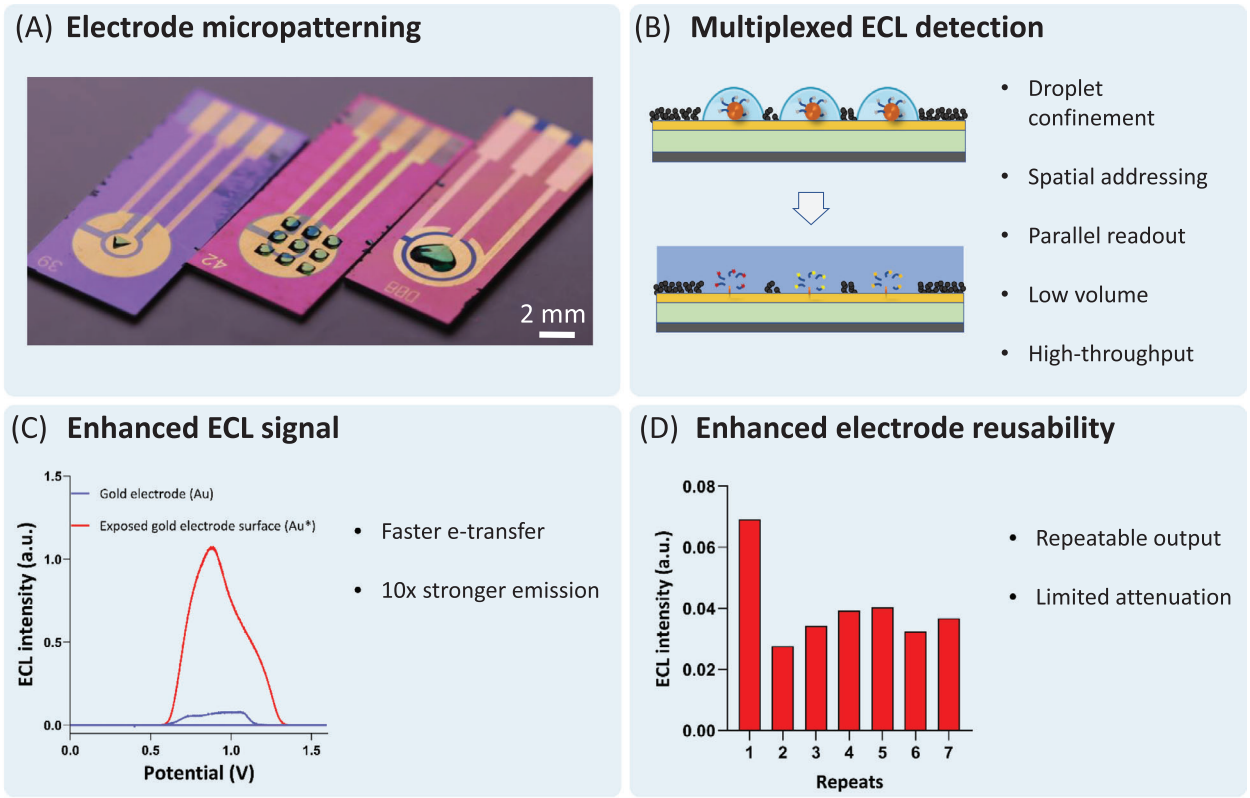

FIGURE 1 | Overview of the novel silica-based coating for ECL-active gold electrode. The coating enables (A) precise electrode micropatterning, (B) spatially resolved and multiplexed ECL detection through droplet confinement in specific regions on the electrode surface, (C) up to 10-fold enhancement in ECL emission due to accelerated electron transfer, and (D) signal reproducibility across repeated measurements.

wavelength: 330–400 nm and UVC wavelength: 230–285 nm, 12 mW cm^{-2}, 90 s), which photo-grafted PFDT onto the vinyl groups rendering the surface superhydrophobic. To introduce spatially controlled functionality, the hydrophobic coating was then selectively ablated using UV exposure through a photomask (UVA wavelength: 330–400 nm and UVC wavelength: 230–285 nm, 50 mW cm^{-2}, 30 min). Regions exposed to light underwent photodegradation of PFDT and oxidative modification of the underlying silica matrix, producing hydroxyl- and carboxyl- rich, hydrophilic domains while the masked areas remained fluorinated and superhydrophobic. Once hydroxyl groups had been generated, the patterned hydrophilic regions were covered with 1 M NaOH (3 min), while the surrounding superhydrophobic surface was protected by filling it with hexane. This hydrolyzed the silica-based coating in the hydrophilic parts (Figure S3). Finally, rinsing the whole chip with water removed the hydrolyzed silica in the ablated regions, thereby exposing clean gold surfaces embedded within the intact superhydrophobic silica matrix. These freshly uncovered electrode sites provide direct electrical access and enable spatially resolved electrochemiluminescence measurements.

2.2 | Characterization of the Electrode Surface at Different Stage

To verify each modification step and to elucidate the structural evolution of the electrode surface, we performed systematic characterization of the original electrode, the silica-coated hydrophobic electrode, and the electrode after selective NaOH-assisted removal of the coating. Water contact angle (WCA) measurements, cross-sectional and top-view SEM, and AFM height mapping were used to correlate surface chemistry with nanoscale morphology.

The original gold electrode (hereafter referred to as "Au") displayed a relatively smooth and homogeneous surface. Cross-sectional SEM clearly delineated the top gold layer from the underlying PECVD-deposited SiO_2 support (Figure 3B) while top-view SEM revealed isolated bright crystallites originating from the chip fabrication process (Figure 3C). AFM measurements showed a low RMS roughness (Sq) of 73 ± 8 nm, consistent with a flat metallic surface. The WCA is at 92.3 ± 1.9° at this stage.

The electrode with superhydrophobic coating (hereafter referred to as "Au@SH") underwent a pronounced transformation. A continuous and densely packed nanoparticle layer uniformly covered the gold surface, as evidenced by top-view SEM (Figure 3G), with only minor uncoated regions occasionally visible. Cross-sectional SEM revealed a porous film with an average thickness of 379 ± 36 nm (Figure 3F). AFM analysis showed a substantial increase in surface roughness from 6 ± 0.6 to 73 ± 8 nm due to the nanostructured coating, resulting in a characteristic granular topography (Figure 3H). This morphological change, together with the fluorinated PFDT grafting, resulted in an increase of the static WCA of 159.9 ± 1.4°, signifying a transition to a superhydrophobic state driven by synergistic micro/nano-roughness and low-surface-energy chemistry.

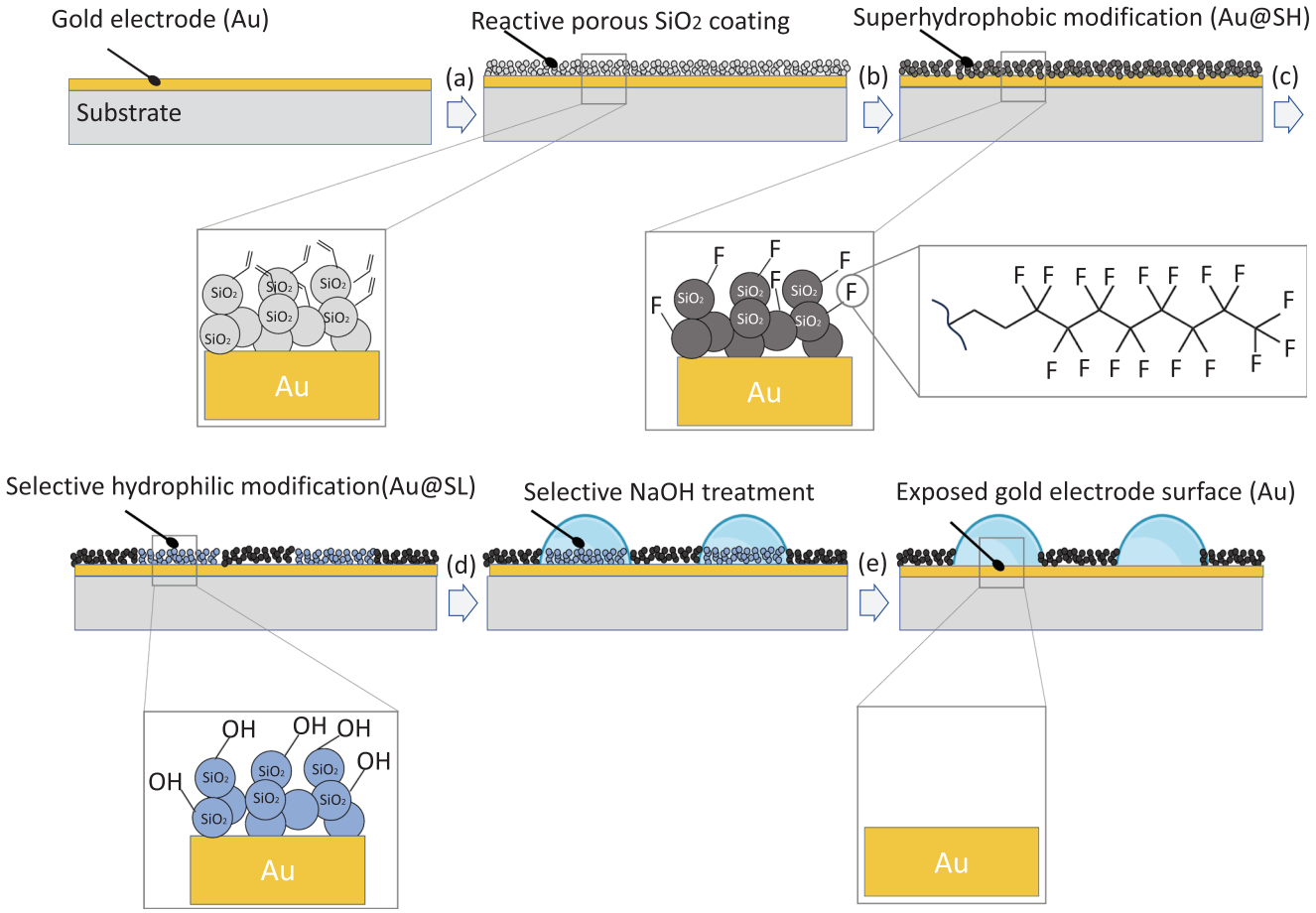

FIGURE 2 | Fabrication workflow of the patterned silica-based coating on gold electrodes. (a) Vinyl-functionalized silica nanoparticles are spray-coated onto the gold working electrode. (b) A 1H,1H,2H,2H-perfluorodecanethiol (PFDT) solution is applied and photochemically grafted onto the vinyl groups under UV irradiation (12 mW/cm^2, 90 s) to form a superhydrophobic property. (c) Selective UV ablation (50 mW/cm^2, 30 mins) through a photomask (Figure S2) removes PFDT and introduces hydrophilic hydroxyl/COOH functionalities in the exposed domains. (d) The hydroxylated regions are briefly treated with 1 M NaOH (3 min) to hydrolyze and weaken the silica particles. The surface is immersed in hexane to selectively protect the hydrophobic regions. (e) Final rinsing in water removes the hydrolyzed silica in the treated areas, revealing clean gold electrode surface surrounded by a superhydrophobic coating for spatially resolved ECL detection.

After selective UV ablation and partial removal of the coating in the patterned regions, the underlying gold surface re-emerged (hereafter referred to as "Au*"). SEM top-view images showed that nanoparticles were no longer detectable in the ablated zones (Figure 3K), and the morphology closely resembled that of the original electrode. AFM confirmed a significant reduction in surface roughness from 73 ± 8 to 31 ± 4 nm within these exposed regions, indicating effective removal of the silica layer and restoration of the exposed gold surface. Consistent with this structural regeneration, static WCA values showed very low water contact angles (<10°), with droplets spreading immediately, demonstrating the return to a hydrophilic surface suitable for direct electrochemical interaction.

An XPS analysis was also performed in order to correlate the surface atomic composition with the characterized morphological changes. Table 1 reports the surface chemical composition determined by analyzing XPS profiles. Compared to the electrode with superhydrophobic modification (Au@SH) the exposed gold electrode surface (Au*) exhibits a sharp decrease in Si (from 17.2% to 0.5%) and F (from 28.3% to 3.1%), accompanied by a substantial increase in Au (from 5.8% to 66.2%). In addition, C and O contents decrease, demonstrating the effectiveness of the NaOH treatment.

The high-resolution XPS spectra, presented in Figure S9, are dominated by the Au 4f regions across all samples. These exhibit the characteristic doublets at ~84.0 eV ($4f_{7/2}$) and ~87.7 eV ($4f_{5/2}$) of metallic gold. The overall intensity of Au band is significantly increased after the silica-coated electrode cleaning by sodium hydroxide. Delving into the C 1s spectra reveals a striking feature: the silica-NPS-functionalized sample, incorporating the F-containing species, displays a highly pronounced oxidized carbon phase, as evidenced by the contributions centered at ~290–294 eV (consistent with carbonyl or carboxylate functionalities). Meanwhile, the O 1s and F 1s and Si 2p regions show generally consistent binding energies across all samples, with an intensity reduction after the treatment and only a subtle ~0.3 eV shift in the most oxidized specimen.

Taken together, the surface characterization results verify the controlled modulation of surface chemistry and nanoscale morphology during fabrication. The patterned electrodes comprise

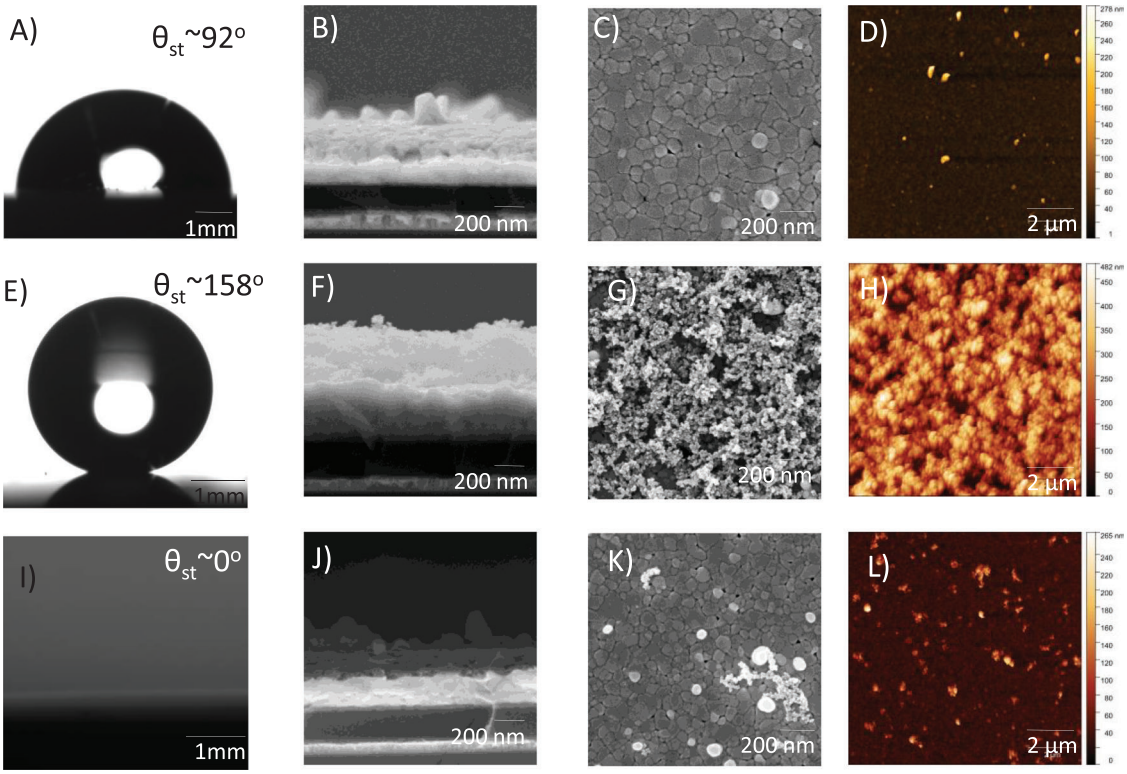

FIGURE 3 | Surface characterization of the gold electrode (Au), the electrode with superhydrophobic modification (Au@SH), and the exposed gold electrode surface (Au*) after NaOH treatment. Rows (A–D), (E–H), and (I–L) correspond to (1) the original gold electrode (Au), (2) the silica-coated electrode after hydrophobic modification (Au@SH), and (3) the silica-coated electrode after NaOH treatment (Au*), respectively. Columns show: water contact angles (col. 1), cross-sectional SEM (col. 2), top-view SEM (col. 3), and AFM height maps (col. 4).

TABLE 1 | Surface atomic composition (%) determined by XPS analysis for the bare gold electrode (Au), superhydrophobic modification (Au@SH), and exposed gold surface (Au*).

Sample Type	Au (%)	O (%)	C (%)	Si (%)	F (%)
Gold electrode (Au)	26.7	24.4	48.9	—	—
Superhydrophobic modification (Au@SH)	5.8	27.2	21.5	17.2	28.3
Exposed gold electrode surface (Au*)	66.2	18.2	12.0	0.5	3.1

hydrophilic, gold-exposed regions surrounded by hydrophobic silica-coated areas, allowing confinement of aqueous droplets and localized electrochemiluminescence signal generation in spatially separated regions.

2.3 | Beads-Based ECL Immunoassay from Modified Electrode

Given the previous surface characterizations, we further investigated the resulting ECL response of the various surface modifications, to enable a preliminary comparison of the performance of the different electrodes' coatings and to identify the optimal ECL pathway and coreactant conditions (tri-*n*-propylamine, TPrA), for potential applications in real-assay scenarios. A tris(2,2′-bipyridyl) ruthenium (II) ($[Ru(bpy)_3]^{2+}$)-labeled magnetic beads (Ru@MB, Figure 4A) has been selected as the ECL-active system of choice, considering that this type of assay is widely used also in commercial clinical tests, in combination with the widely employed TPrA as coreactant. Ru@MB were used in the first detection strategy. They were prepared by covalently attaching the $Ru(bpy)_3^{2+}$ luminophore directly to the surface of magnetic microbeads. This configuration provides a rapid, reagent-minimal readout strategy in which the ECL originates directly from the $[Ru(bpy)_3]^{2+}$-tagged beads without requiring additional biomolecular assembly [51, 52] (Figure 4A). An external magnet positioned beneath the chip immobilized the beads at the electrode surface, ensuring stable positioning during ECL excitation. Under an applied anodic potential, tri-*n*-propylamine (TPrA) is oxidized at the electrode to yield the radical cation $TPrA^{\bullet+}$, which rapidly deprotonates to form the strongly reducing $TPrA^{\bullet}$ radical. This species reduces $[Ru(bpy)_3]^{2+}$ to $[Ru(bpy)_3]^{+}$, which is subsequently oxidized to its excited state $[Ru(bpy)_3]^{2+*}$ via electron transfer with $TPrA^{\bullet+}$. Radiative relaxation of $[Ru(bpy)_3]^{2+*}$ produces the characteristic luminescence recorded during detection.

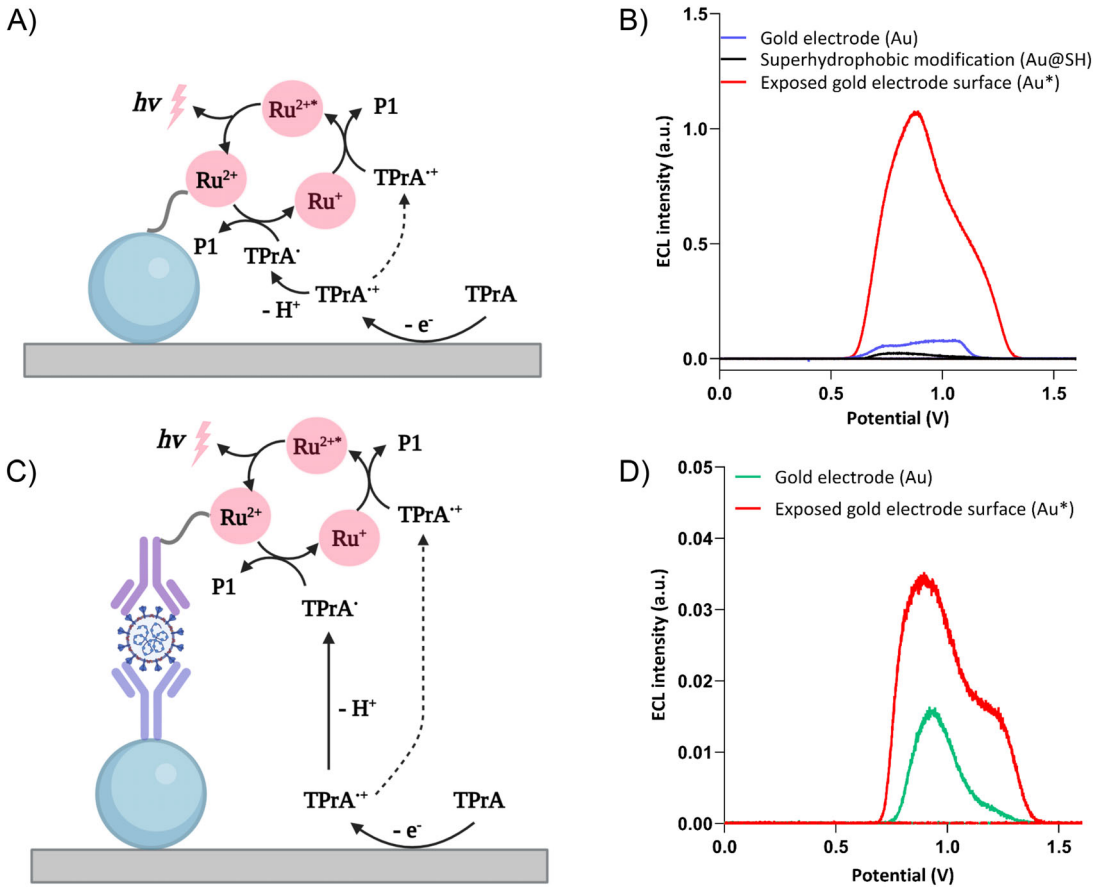

FIGURE 4 | (A) Schematic illustration of the Ru-labeled magnet microbead-based(Ru@MB) ECL. (B) ECL intensity of the original, coated, and modified electrodes with Ru@MB. (C) Schematic illustration of the magnet microbead-based ECL immunoassay (Ab@MB and Ab-Ru) for SARS-CoV-2 detection. (D) ECL intensity of the NaOH-cleaned electrode and modified electrode with 10 000 cps/mL of SARS-CoV-2.

It was demonstrated that this ECL luminophore/coreactant combination was effectively able to provide a consistent signal enhancement upon employing the electrode subjected to NaOH-assisted removal of the coating (Figure 4SB), in comparison to the hydrophilic hydroxy-functionalized and carboxyl-functionalized silica-coated electrode (Figure S4C,D). Accordingly, NaOH-assisted selective coating removal was applied in all subsequent experiments. We hypothesize that this signal enhancement is a joint effect of the carbonaceous contamination reduction [53], oxide removal and further exposure of the gold surface and increase of the electron transfer kinetics which governs TPrA oxidation [54, 55]. Since TPrA is used as co-reactant for the ECL system, the apparent heterogeneous rate constant of electron transfer (k_{ET}) for TPrA oxidation on both original and modified electrode surfaces was further studied for rationalize the ECL enhancing effect by the electrochemical impedance spectroscopy (EIS) measurements (Figures S5 and S6) [56]. The values of the original electrode and modified electrode were 0.004 and 0.011 cm s^{-1}, respectively. These results confirm that the significant difference in ECL signal is a direct result of the k_{ET} rate of modified electrode being higher than that of the original electrode (corresponding histogram Figure S7A). Therefore, with these preliminary results in mind, we moved to the investigation of the patterned electrodes (comprising hydrophilic, gold-exposed regions surrounded by hydrophobic silica-coated areas), in order to further demonstrate ECL sensing, upon employing two complementary strategies that operate within the spatially confined hydrophilic zones.

In the second detection mode (Figure 4C), a full sandwich immunoassay was constructed on magnetic microbeads functionalized with biotinylated capture antibodies (Ab@MB). After magnetic immobilization in the designated hydrophilic zones, synthetic SARS-CoV-2 spike protein was added as a model target and selectively bound to the capture antibodies. A $[Ru(bpy)_3]^{2+}$-labeled secondary antibody was subsequently introduced to complete the sandwich structure. Through this dual-antibody recognition, the assay achieves high specificity, while the $[Ru(bpy)_3]^{2+}$ label provides the necessary luminophore for ECL readout. Each hydrophilic domain therefore functions as an independent reaction well in which different targets or different immunoassay configurations can be probed simultaneously [51, 57].

Despite the difference in assembly, both detection modes (Ru@MB and Ab@MB) rely on the same electrochemiluminescence mechanism, as illustrated in Figure 4A,C. Because both direct magnet microbead-based ECL and sandwich-format ECL converge on this pathway, the emission mechanism remains identical, differing only in how the Ru(II) luminophore is presented at the electrode interface. The emitted photons are captured and is proportional to the analytes concentration.

To further evaluate analytical performance, we tested both the original electrode and the modified electrode on the ECL sandwich immunoassay using synthetic SARS-CoV-2 spike protein samples (Figure 4C). As shown in Figure 4D, the modified electrode exhibited better performance for magnet microbead-based immunoassay due to the higher k_{ET} rate of TPA oxidation. The observed signal amplification is further quantified by a metric called signal gain, which is calculated as:

$$SG\ (\%) = \frac{I_{ecl} - I_{ecl0}}{I_{ecl0}} \times 100 \quad (1)$$

where I_{ecl} represents the ECL signal from the modified electrode, and I_{ecl0} represents the ECL signal from the original electrode.

As a result, the signal gain is 116%, which further emphasizes the superior signal amplification capability of the modified electrode compared to the original electrode. The corresponding histogram (Figure S7B) demonstrates clear discrimination between the original electrode and the modified electrode in the control and 10000 cps/mL of SARS-CoV-2 samples, indicating that the modified electrode provides superior analytical sensitivity and a significantly improved signal-to-background ratio.

In addition, the operational stability of the modified electrode was assessed through repeated potential-sweep measurements. As shown in Figure S7C, the ECL intensity remained stable across multiple cycles, with only minimal signal loss. This behavior demonstrates that the coating forms a mechanically and chemically durable interfacial layer that protects the gold surface from fouling and preserves electrochemical activity during repeated measurements.

2.4 | Spatially Resolved Beads-Based Assay on Patterned Electrode and Calibration

For spatially resolved detection, ECL imaging was applied to evaluate the performance of the ECL distribution into the microarrays with the patterned electrode, as this will facilitate the protocols optimization for simultaneous detection of various target analytes. The patterned silica-gold electrode allows spatially resolved and parallel electrochemiluminescent detection over a multiplicity of hydrophilic compartments. To prove this capacity for multiplexing, we first examined a 4-channel microarray, in which Ru@MB were deliberately placed in the upper-left and lower-right hydrophilic spots only (Figure 5C). Upon applying the ECL excitation potential, the corresponding emission map in Figure 5D indicates bright, spatially confined signals only at the two targeted locations, while the remaining spots -without Ru@MB- display practically no background emission. The one-to-one correspondence in the local ECL output, such as representative placement of the sample, indicates that the patterned architecture has prevented lateral diffusion, thus maintaining spatial registration of the biochemical signal.

This principle was expanded to a larger 14-channel microarray to demonstrate higher-order multiplexing capability. In this configuration, all hydrophilic spots were filled with Ru@MB, as shown in the bright-field image in Figure 5E. After voltage application, the ECL emission map in Figure 5F showed an evenly distributed luminescent spot over the array corresponding to a single detection zone for each of the spots. Since the position fidelity was apparent and the signal intensities were consistent, the microarray allowed for parallel analysis in many reaction chambers without cross-talk or loss of spatial definition.

Thus, these results validate the patterned silica-coated electrode as a robust platform for spatially confined ECL sensing, with individual microreactors in each hydrophilic compartment. The spatially resolved optical output directly correlates with sample placement, allowing for parallel analyses of multiple analytes on a single, small chip [57].

Furthermore, a simulated beads-based immunoassay was constructed to evaluate the applicability of the platform in such detection. In order to mimic the real assay, biotinylated Ru-labeled antibodies functionalized with streptavidin-coated magnetic beads (Ab-Ru@MB) has been used. The streptavidin–biotin interaction enables controlled immobilization of Ru-labeled antibodies on the bead surface while maintaining a constant bead concentration. By varying the concentration of Ru-labeled antibodies during the functionalization step, the number of luminophores per bead can be systematically tuned while keeping the bead number constant. This strategy allows the direct investigation of the relationship between luminophore loading and ECL intensity in bead-based assays [58, 59]. By keeping constant the beads concentration in the different active area of the micropatterning electrode we investigated different concentrations of Ab-Ru using two 2-channel microarray electrodes. As displayed in Figure 5A, the microchannels were filled with 0.3 (left) and 1 nM (right) of Ab-Ru@MB. After applying the ECL excitation potential, the corresponding emission map in Figure 5B indicates different intensities of bright emission. As displayed in Figure 5G–J, the microchannels with 0, 0.1, 0.3, and 1 nM of Ab-Ru exhibited gradually increasing bright emission. The integrated ECL intensity was linear with the Ab-Ru concentration in the range from 0 to 1 nM with a limit of detection (LOD) of 0.1 nM (Figure 5K). The purpose of this experiment was to obtain a spatially resolved calibration curve from a single ECL image. The limited number of data points reflects a practical compromise imposed by the electrode design. In particular, the patterned area must be sufficiently large to generate a detectable ECL signal, but not excessively large, since increasing the electrode area would also increase the ohmic drop and negatively affect the electrochemical/ECL response. Conversely, further subdividing or reducing the patterned area to accommodate additional Ab-Ru concentrations would significantly decrease the signal intensity and compromise measurement reliability. Therefore, the four selected concentrations were chosen to cover the relevant concentration range while maintaining an adequate balance between ECL signal intensity, electrode geometry, and ohmic-drop limitations. The patterned electrode with microchannels enables spatially resolved detection in assays, confirming its effectiveness for simultaneous quantification of multiple analytes.

3 | Conclusion

In this work, a silica nanoparticle–based surface engineering strategy was developed to enable spatially resolved electrochemiluminescence (ECL) detection on gold electrodes.

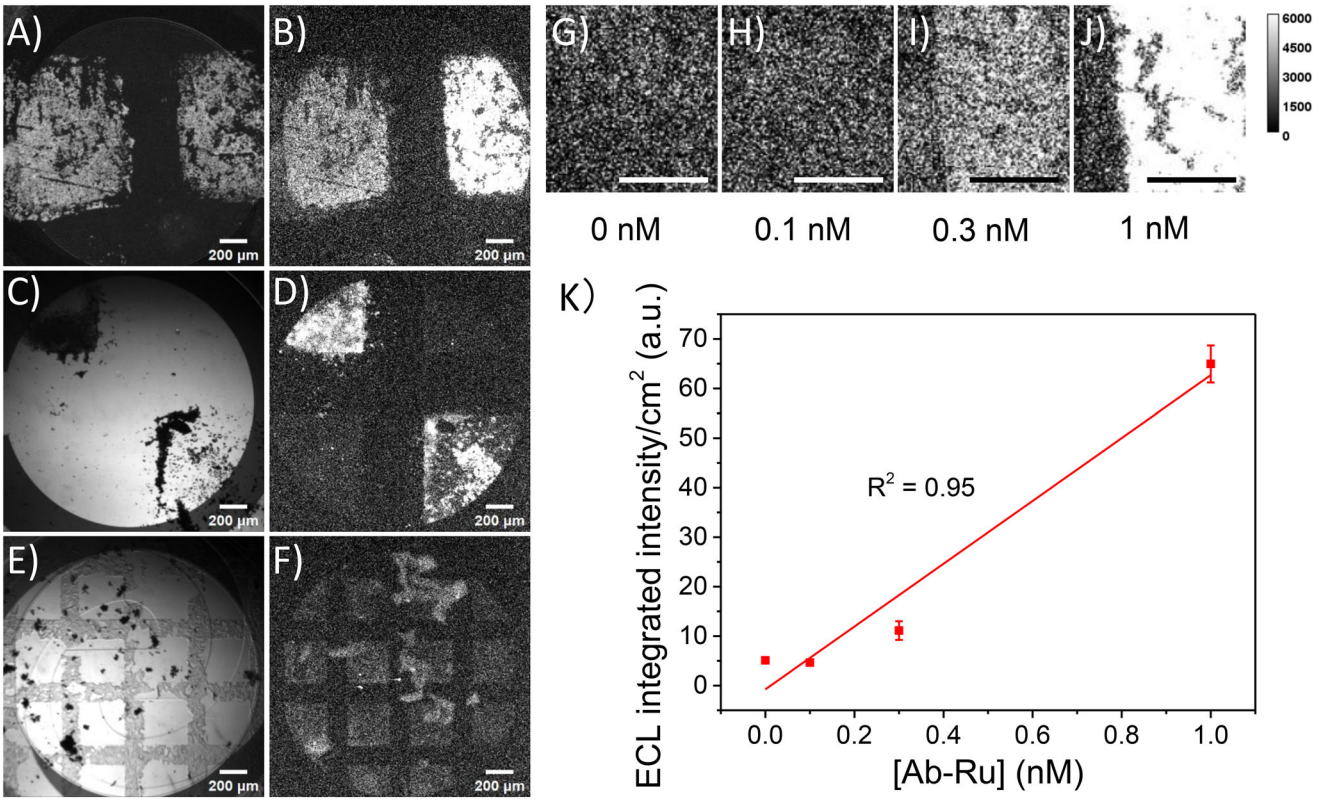

FIGURE 5 | Spatially resolved ECL detection using patterned microarrays. (A) Bright-field image of the 2-channel (1 mm × 1 mm square) microarray before voltage application (B) Corresponding ECL emission map for 2-channel microarray after voltage application. (C) Bright-field image of the 4-channel (1 mm × 1 mm square) microarray before voltage application, with Ru-labeled magnetic microbeads (Ru@MB) added only to the upper-left and lower-right spots. (D) Corresponding ECL emission map for 4-channel microarray acquired after voltage application. (E) Bright-field image of the 14-channel microarray before voltage application, with samples added to all hydrophilic spots. (F) Corresponding ECL emission map for 14-channel (330 μm × 330 μm square) microarray acquired after voltage application. (G–J) ECL image of 0 nM /0.1 nM /0.3 nM/1 nM of Ab-Ru@MB on the patterned electrode scale bar: 200 μm. Image were generated from the raw image stacks using a Z-projection (sum of slices 40–70) in ImageJ. (K) Calibration curve of ECL intensity versus Ab-Ru@MB concentration.

Comprehensive surface characterization (SEM, AFM, XPS, and WCA) confirmed controlled modulation of surface morphology and chemistry throughout each fabrication step. Notably, NaOH-assisted treatment was found to be essential not only for removing the silica layer in patterned regions but also for restoring and cleaning the gold surface, thereby significantly altering interfacial properties. Electrochemical impedance spectroscopy revealed a pronounced decrease in charge-transfer resistance, accompanied by an increase in the apparent TPrA oxidation electron-transfer rate constant from 0.004 to 0.011 cm s^{-1}, which directly correlated with the observed enhancement in ECL intensity. These results demonstrate that signal amplification arises primarily from improved electron-transfer kinetics rather than geometric molecular confinement, providing mechanistic insight into the role of interfacial surface engineering in ECL systems. However, in this very preliminary work we should notice that due to the weak interaction between silica nanoparticle and gold surface, direct mechanical force can easily damage the coating, which will lead to bad special confinement and cross contamination. Operation with caution is needed.

Under optimized conditions, the modified electrodes exhibited up to a tenfold increase in emission compared to bare gold electrodes, along with improved signal stability upon repeated measurements. The platform was fully compatible with magnetic microbead–based immunoassays, enabling both direct detection of Ru-labeled beads and sandwich-format assays. Spatially resolved ECL imaging using 4-channel and 14-channel patterned arrays was achieved without detectable crosstalk. Quantitative analysis showed a linear response range of 0–1 nM Ab–Ru, with a limit of detection of 0.1 nM.

Beyond proof-of-concept demonstrations, this study introduces a versatile and scalable approach for engineering spatially addressable ECL interfaces via spray-based nanostructured coatings and photochemical patterning. The platform integrates signal enhancement, surface regeneration, and spatial resolution within a single system, providing a strong foundation for miniaturized droplet microarray–based diagnostics and next-generation multiplexed electrochemical biosensors.

4 | Experimental Section

4.1 | Materials

Chips with gold working electrode were prepared by Swiss Center for Electronics and Microtechnology (CSEM, Neuchâtel, Swiss).

Some preliminary investigations have been performed on commercialized gold–based thin-film single-(micro) electrodes (DSE1-Au; WE: 50/150 nm Ti/Au, 1 mm Ø), purchased by MicruX Technologies. Silica nanoparticles AEROSIL 200 were purchased from Evonik (Essen, Germany). Vinyltrimethoxysilane (VTMS),1H,1H,2H,2H-perfluorodecanethiol (PFDT) and Sodium hydroxide (NaOH) were purchased from Sigma–Aldrich (St. Louis, Missouri, USA). Hydrochloric acid was purchased from Carl Roth (Karlsruhe, Germany) ethanol absolute and n-hexane were purchased from VWR (Darmstadt, Germany). All chemicals were used as received. Analytical grade reagents have been used in this work and ultrapure (Milli-Q) water was used for all experiments. Tri-*n*-propylamine (TPrA, MW = 143.27 g/mol, ≥98% v/v), sodium phosphate monobasic dihydrate ($NaH_2PO_4 \cdot 2H_2O$, MW = 156.01 g/mol, ≥99%), sodium phosphate dibasic (Na_2HPO_4, MW = 141.96 g/mol, ≥99.5%), phosphoric acid (H_3PO_4, MW = 98.00 g/mol, ≥85%), potassium persulfate ($K_2S_2O_8$, MW = 270.32 g/mol, >99%) and ethanol (C_2H_6O, MW = 46.07 g/mol, 100%) were purchased from Sigma-Aldrich (St. Louis, Missouri, USA). 2.8 µm polystyrene magnetic beads covalently linked to $[Ru(bpy)_3]^{2+}$ were purchased from Roche Diagnostics. For the ECL immunoassay, Human Anti-SARS-CoV-2 Spike RBD Antibody-coupled Magnetic Beads was purchased from ACRO-Biosystems (Newark, DE, USA). AMPLIRUN TOTAL SARS-CoV-2 CONTROL (inactivated coronavirus SARS-CoV-2 formulated in viral transport medium) was bought from Vircell Microbiologists (Granada, Spain). SARS-CoV-2/2019-nCoV Spike Antibody (Rabbit PAb) was obtained from Sino Biological Europe GmbH (Eschborn, Germany). For microscopic imaging, an epifluorescence microscope from Nikon (Chiyoda, Tokyo, Japan) equipped with an ultrasensitive EMCCD camera (EM-CCD 9100−13 from Hamamatsu, Japan) was used with a resolution of 512 × 512 pixels and a size of 16 × 16 µm^2.

4.2 | Preparation of Vinyl-Functionalized Silica Coating

Silica nanoparticle (375 mg) was dispersed in 45 mL of absolute ethanol. The mixture was sonicated (Sonoplus HD 4100, Berlin, Germany) for 30 min and then 510 µL VTMS and 300 µL Hydrochloric acid was added into the mixture and sonicated for another 60 min. The modified silica dispersion was spray-coated by EaxactaCoat(Sono-Tek, New York, USA) onto pre-cleaned gold electrodes. The pre-clean was done by UVO Cleaner, model 42–220 (Jetlight Co. Inc., Ivring, USA) and after coating the electrodes were annealed on IKA C-Mag hotplate stirrers C-MAG HS4(Staufen im Breisgau, Germany) at 150°C for 1 h. The size of the vinyl functionalized silica nanoparticles was measured through Dynamic light scattering by Malvern Zetasizer Nano ZS (Malvern Instruments GmbH, Herrenberg, Germany).

4.3 | Surface Patterning via Photomask Ablation and NaOH Treatment

The silica-coated electrodes were first rendered hydrophobic with 10% v/v PFDT isopropanol solution under UV irradiation by UVACUBE 2000 with Mercury bulb (Honle uv technology, Gilching, Germany) for 90 s with both UVA and UVC intensity around 6 mW/ cm^2 to induce thiol–ene click reactions. The UVA (wavelength: 330–400 nm) and UVC (wavelength: 230-285 nm) intensity were measured by UVA/UVC sensors (Honle UV Technology, Gilching, Germany) Photopatterning was performed by UV exposure through a chrome photomask (ROSE FOTOMASKEN, Bergisch Gladbach,Germany) with square pattern in the size of 330 µm × 330 µm under UV irradiation for 30 min with both UVA and UVC intensity at 50 mW/ cm^2. The exposed (ablated) areas became hydrophilic. The electrodes were contacted with 1 M NaOH water solution by discontinuous dewetting and placed in hexane for 3 min to selectively remove the silica layer in the hydrophilic regions. In the process the NaOH water solution are attached to the hydrophilic spots while the hydrophobic parts are protected by the hexane from removal.

4.4 | Characterization

The morphology of the silica-coated electrodes was characterized by Zeiss LEO 1530 Gemini scanning electron microscopy (Carl Zeiss, Germany) in both top-view and cross-sectional modes. Coating thickness was determined using cross-sectional SEM images and quantified in ImageJ using the Measure → Analyze functions. Three independent samples were analyzed, and for each sample three measurements were taken; the reported thickness corresponds to the calculated mean value.

In the measurement of water contact angles (WCA), the shape of the droplet containing 3 µL of DI water was measured by means of a DSA25 drop shape analyzer provided by Krüss (Hamburg, Germany). The static water contact angle was then measured by placing the droplet onto the surface until equilibrium.

Atomic force microscopy Type AFM; NTEGRA scanning probe microscope (NT-MDT, Russia) was used to measure nanoscale surface roughness and compare the morphology of gold, coated regions, and NaOH-treated hydrophilic surfaces. Measurements were performed in tapping (semi-contact) mode to minimize tip–sample interaction forces. AFM images were collected over a scan area of 10 µm × 10 µm under ambient conditions. Silicon probes NT-MDT NSG10 (High Resolution Silicon AFM Cantilevers), with a nominal resonance frequency range of 140–390 kHz and a spring constant between 3.1 and 37.6 N m^{-1}, were employed for all analyses. AFM data processing and image analysis were carried out using Gwyddion software.

To confirm the selective removal of the silica layer, X-ray Photoelectron Spectroscopy (Thermo Scientific K-Alpha XPS; Waltham, MA, USA) was performed on both coated and NaOH-treated regions. The instrumentation was equipped with a monochromatic Al-Kα source (1486.6 eV), operating in constant analyzer energy (CAE) mode. The pass energy was 20 eV for high-resolution spectra with a spot size of 400 µm.

4.5 | Electrochemiluminescence (ECL) Measurements

Concerning the preliminary results, in a typical ECL measurement procedure, the Ru-labelled MMBs suspension was drop casted onto a gold–based thin-film single-(micro)electrode. Beads were magnetically concentrated onto the WE surface using a

magnet placed underneath, and a Pt wire has been used as the CE, while an Ag filament has been used as the RE. This three-electrode system was placed in a All-in-One cell (Ref. ED-AIO-CELL, MicruX Technologies) and housed in a dark box to eliminate interference from ambient light. The cell was carefully placed as close as possible to the PMT (H13543-20, Hamamatsu Photonics K.K., Japan), which was positioned over the WE. The ECL signal intensity was obtained upon triggering the system with a CV scan. More in detail, CV–ECL plots were collected by scanning the working electrode potential at 100 mV/s from open circuit potential (OCP) either down to −2.5 V, when using $K_2S_2O_8$ as the coreactant, or up to 2.5 V, when using TPrA as the coreactant, then back to 0 V (vs. Ag) and, eventually, terminating the cycle at OCP. The solution emission during CV–ECL measurements was acquired every 100 ms through the PMT, whose voltage was set to 750 mV, and amplified with a Keithley Model 6485 Picoammeter (Keithley Instruments Inc., United States). ECL spectra were collected by a SEC2000 spectra system UV–vis spectrophotometer (ALS Co. Ltd., Japan).

Electrochemiluminescence (ECL) measurements were carried out using a photomultiplier tube (PMT; Hamamatsu H13543-20, Hamamatsu Photonics, Japan) positioned directly above the working electrode to record the emitted light intensity. The electrochemical control and potential excitation for ECL generation were provided by a potentiostat (BioLogic SP-150e, BioLogic Science Instruments, France). Electrical signals and amplification settings were monitored using a KEITHLEY 6485 Pico ammeter (Tektronix/Keithley Instruments, USA), which was used to display the applied current amplification level during the measurements. All electrochemical experiments were performed using EC-Lab V11.52 software (BioLogic, France), which was used for data acquisition, synchronization of PMT signal recording with applied potential, and post-measurement analysis. Cyclic voltage scan from 0 V to +1.6 V with scan rate 100mV/s was applied. A standard three-electrode configuration was employed, with the gold electrode as the working electrode, a silver wire reference, and a platinum wire as the counter electrode.

4.6 | Covalent Functionalization of Ru-Labeled Magnet Microbead-Based (Ru@MB)

First, 217 µL of beads stock suspension (0.72 $mg{\cdot}mL^{-1}$) were washed three times with PBS buffer using a magnetic support. Subsequently, the Ruthenium N-hydroxysuccinimide solution (2.7×10^{-2} $mg{\cdot}mL^{-1}$) was added and stirred overnight. After incubation, the beads were washed with PBS for 5 times using magnetic support. Finally, Ru@MB were suspended in 217 µL of PBS to maintain the original bead concentration.

4.7 | Immunoassay Protocol (Ab@MB)

The immunoassay design involves the following components: i) Magnetic beads functionalized with anti-RBD (S1 Spike) antibodies to capture the SARS-CoV-2 virus. These beads are pre-treated with BSA to minimize non-specific binding, ii) SARS-CoV-2 virions: the (inactivated) target virus particles that will be detected by the assay, iii) Probe: Ru-labeled detection antibody (Ab-Ru) was prepared according to the previously reported protocol [59]. The probe binds specifically to the captured virus particles.

The immunoassay procedure was performed using a magnetic bead-based platform. First, 6.0 µL of magnetic bead solution (1 mg/mL) was added to each eppendorf tubes and subsequently washed twice. To minimize nonspecific binding, the beads were blocked by incubating with 200 µL of blocking buffer for 30 min at room temperature, followed by another two washes.

For target detection, SARS-CoV-2 virions and Ru-labeled detection antibody were then added, the total volume adjusted to 250 µL with washing buffer, and the mixture incubated for 10 min at room temperature to facilitate binding. After two washes to remove unbound materials, the beads were resuspended in 6 µL of washing buffer for ECL measurement.

4.8 | Spatially Resolved Beads-Based Assay Protocol (Ab-Ru@MB)

Antibody labeled with biotin and $[Ru(bpy)_3]^{2+}$ (Ab-Ru) derived from the SAP assay (R2) was prepared according to the previously reported protocol [57, 60].

These antibodies were employed to functionalize streptavidin-coated magnetic beads (2.8 µm, Dynabead, Thermo-Fisher Scientific). In brief, beads at the same initial concentration were washed with PBS (pH 7.4), incubated with different concentrations of Ab-Ru for 3 h at 37°C, washed to remove unbound antibody, and resuspended in PBS to maintain the original bead concentration (0.72 $mg{\cdot}mL^{-1}$).

For the multiplexed assay, beads with different concentrations of Ab-Ru were introduced onto patterned electrodes by pipetting into designated wells. ECL images were acquired from each patterned region under identical electrochemical stimulation. Figure S10 is the actual photograph of the electrochemical cell for ECL imaging.

Author Contributions

As per the CReDiT terminology, Y.S.: Formal Analysis, Investigation, Methodology, Data curation, Visualization, Writing – Original Draft Preparation, Writing – Review & Editing. T.S.: Formal Analysis, Investigation, Methodology, Data curation, Visualization, Writing – Review & Editing. M.X.: Investigation, Methodology, Data curation, Visualization, Writing – Review & Editing. M.V.B.: Investigation, Methodology, Data curation, Visualization, Writing – Review & Editing. E.L.S.: Investigation, Methodology, Data curation, Visualization, Writing – Review & Editing. G.G.: Investigation, Methodology, Data curation, Visualization, Writing – Review & Editing. V.P.: Investigation, Methodology, Data curation, Visualization, Writing – Review & Editing. C.C.: Investigation, Methodology, Data curation, Visualization, Writing – Review & Editing. E.F.: Investigation, Methodology, Data curation, Visualization, Writing – Review & Editing. S.C.: Funding Acquisition, Resources, Supervision, Writing – Review & Editing. L.P.: Funding Acquisition, Resources, Supervision, Writing – Review & Editing. G.V.: Conceptualization, Methodology, Resources, Supervision, Validation, Writing – Review & Editing. P.A.L.: Conceptualization, Funding Acquisition, Resources, Supervision, Validation, Writing – Review & Editing.

Acknowledgements

Open access funding enabled and organized by Projekt DEAL.

[Correction added on June 11, 2026, after first online publication: funding statement has been updated.]

Funding

The European Union's Horizon Europe EIC Pathfinder Open program "ECLIPSE" (Grant Agreement No. 101046787) is acknowledged for financial support.

Conflicts of Interest

The authors declare no conflicts of interest.

Data Availability Statement

All data needed to evaluate the conclusions in the paper are present in the paper. Additional data available upon request or in RADAR4KIT repository: https://doi.org/10.35097/k97kwkqzdx37n9m1.

References

1. World Health Organization, "Global Health Estimates: Life Expectancy and Leading Causes of Death and Disability," (2025), https://www.who.int/data/gho/data/themes/mortality-and-global-health-estimates.

2. Institute for Health Metrics and Evaluation, "Global Burden of Disease (2024): Ith minor Processing by Our World in Data. ″Deaths from Infectious Diseases", https://ourworldindata.org/grapher/deaths-from-infectious-diseases.

3. Y. Hu, J. Guo, G. Li, et al., "Role of Efficient Testing and Contact Tracing in Mitigating the COVID-19 Pandemic: A Network Modelling Study," *BMJ Open* 11, no. 7 (2021): 045886, https://doi.org/10.1136/bmjopen-2020-045886.

4. Y. Cui, S. Ni, and S. Shen, "A Network-based Model to Explore the Role of Testing in the Epidemiological Control of the COVID-19 Pandemic," *BMC Infectious Diseases [Electronic Resource]* 21, no. 1 (2021): 58, https://doi.org/10.1186/s12879-020-05750-9.

5. R. K. Saiki, S. Scharf, F. Faloona, et al., "Enzymatic Amplification of Beta-globin Genomic Sequences and Restriction Site Analysis for Diagnosis of Sickle Cell Anemia," *Science* 230, no. 4732 (1985): 1350–1354, https://doi.org/10.1126/science.2999980.

6. S. A. Bustin, "Absolute Quantification of mRNA Using Real-time Reverse Transcription Polymerase Chain Reaction Assays," *Journal of Molecular Endocrinology* 25, no. 2 (2000): 169–193, https://doi.org/10.1677/jme.0.0250169.

7. S. Yang and R. E. Rothman, "PCR-based Diagnostics for Infectious Diseases: Uses, Limitations, and Future Applications in Acute-care Settings," *The Lancet Infectious Diseases* 4, no. 6 (2004): 337–348, https://doi.org/10.1016/S1473-3099(04)01044-8.

8. M. Kubista, J. M. Andrade, M. Bengtsson, et al., "The Real-time Polymerase Chain Reaction," *Molecular Aspects of Medicine* 27, no. 2-3 (2006): 95–125, https://doi.org/10.1016/j.mam.2005.12.007.

9. S. A. Bustin, V. Benes, J. A. Garson, et al., "The MIQE Guidelines: Minimum Information for Publication of Quantitative Real-time PCR Experiments," *Clinical Chemistry* 55, no. 4 (2009): 611–622, https://doi.org/10.1373/clinchem.2008.112797.

10. A. van Belkum, T. T. Bachmann, G. Lüdke, et al., "Developmental Roadmap for Antimicrobial Susceptibility Testing Systems," *Nature Reviews Microbiology* 17, no. 1 (2019): 51–62, https://doi.org/10.1038/s41579-018-0098-9.

11. P. K. Drain, E. P. Hyle, F. Noubary, et al., "Diagnostic Point-of-care Tests in Resource-limited Settings," *The Lancet Infectious Diseases* 14, no. 3 (2014): 239–249, https://doi.org/10.1016/S1473-3099(13)70250-0.

12. P. Yager, G. J. Domingo, and J. Gerdes, "Point-of-care Diagnostics for Global Health," *Annual Review of Biomedical Engineering* 10 (2008): 107–144, https://doi.org/10.1146/annurev.bioeng.10.061807.160524.

13. P. Kralik and M. Ricchi, "A Basic Guide to Real Time PCR in Microbial Diagnostics: Definitions, Parameters, and Everything," *Frontiers in Microbiology* 8 (2017): 108, https://doi.org/10.3389/fmicb.2017.00108.

14. C. D. Sibley, G. Peirano, and D. L. Church, "Molecular Methods for Pathogen and Microbial Community Detection and Characterization: Current and Potential Application in Diagnostic Microbiology," *Infection, Genetics and Evolution* 12, no. 3 (2012): 505–521, https://doi.org/10.1016/j.meegid.2012.01.011.

15. C. J. Smith and A. M. Osborn, "Advantages and Limitations of Quantitative PCR (Q-PCR)-based Approaches in Microbial Ecology," *Fems Microbiology Ecology* 67, no. 1 (2009): 6–20, https://doi.org/10.1111/j.1574-6941.2008.00629.x.

16. T. Notomi, H. Okayama, H. Masubuchi, et al., "Loop-mediated Isothermal Amplification of DNA," *Nucleic Acids Research* 28, no. 12 (2000): E63, https://doi.org/10.1093/nar/28.12.e63.

17. O. Piepenburg, C. H. Williams, D. L. Stemple, and N. A. Armes, "DNA Detection Using Recombination Proteins," *PLoS Biology* 4, no. 7 (2006): 204, https://doi.org/10.1371/journal.pbio.0040204.

18. I. M. Lobato and C. K. O'Sullivan, "Recombinase Polymerase Amplification: Basics, Applications and Recent Advances," *Trends in Analytical Chemistry* 98 (2018): 19–35, https://doi.org/10.1016/j.trac.2017.10.015.

19. N. Kohmer, C. Rühl, S. Ciesek, and H. F. Rabenau, "Utility of Different Surrogate Enzyme-Linked Immunosorbent Assays (sELISAs) for Detection of SARS-CoV-2 Neutralizing Antibodies," *Journal of Clinical Medicine* 10, no. 10 (2021): 2128, https://doi.org/10.3390/jcm10102128.

20. K. M. Koczula and A. Gallotta, "Lateral Flow Assays," *Essays in Biochemistry* 60, no. 1 (2016): 111–120, https://doi.org/10.1042/EBC20150012.

21. S. Lee, J. S. Park, H. Woo, et al., "Rapid Deep Learning-assisted Predictive Diagnostics for Point-of-care Testing," *Nature Communications* 15, no. 1 (2024): 1695, https://doi.org/10.1038/s41467-024-46069-2.

22. Y. Liu, L. Zhan, Z. Qin, J. Sackrison, and J. C. Bischof, "Ultrasensitive and Highly Specific Lateral Flow Assays for Point-of-Care Diagnosis," *ACS Nano* 15, no. 3 (2021): 3593–3611, https://doi.org/10.1021/acsnano.0c10035.

23. R. Gupta, P. Gupta, S. Wang, et al., "Ultrasensitive Lateral-flow Assays via Plasmonically Active Antibody-conjugated Fluorescent Nanoparticles," *Nature Biomedical Engineering* 7, no. 12 (2023): 1556–1570, https://doi.org/10.1038/s41551-022-01001-1.

24. P. Lasch, W. Beyer, A. Bosch, et al., "A MALDI-ToF Mass Spectrometry Database for Identification and Classification of Highly Pathogenic Bacteria," *Scientific Data* 12, no. 1 (2025): 187, https://doi.org/10.1038/s41597-025-04504-z.

25. M. Grossegesse, F. Hartkopf, A. Nitsche, L. Schaade, J. Doellinger, and T. Muth, "Perspective on Proteomics for Virus Detection in Clinical Samples," *Journal of Proteome Research* 19, no. 11 (2020): 4380–4388, https://doi.org/10.1021/acs.jproteome.0c00674.

26. A. Elbehiry, M. Aldubaib, A. Abalkhail, et al., "How MALDI-TOF Mass Spectrometry Technology Contributes to Microbial Infection Control in Healthcare Settings," *Vaccines (Basel)* 10, no. 11 (2022): 1881, https://doi.org/10.3390/vaccines10111881.

27. J. Rychert, "Benefits and Limitations of MALDI-TOF Mass Spectrometry for the Identification of Microorganisms," *Journal of Infectiology* 2, no. 4 (2019): 1–5, https://doi.org/10.29245/2689-9981/2019/4.1142.

28. S. R. S. Pour, D. Calabria, A. Emamiamin, et al., "Electrochemical vs. Optical Biosensors for Point-of-Care Applications: A Critical Review," *Chemosensors* 11, no. 10 (2023): 546, https://doi.org/10.3390/chemosensors11100546.

29. R. Abbasi, X. Hu, A. Zhang, I. Dummer, and S. Wachsmann-Hogiu, "Optical Image Sensors for Smart Analytical Chemiluminescence,"

Biosensors Bioengineering (Basel) 11, no. 9 (2024): 912, https://doi.org/10.3390/bioengineering11090912.

30. M. M. Richter, "Electrochemiluminescence (ECL)," *Chemical Reviews* 104, no. 6 (2004): 3003–3036, https://doi.org/10.1021/cr020373d.

31. S.-M. Yoo, Y.-M. Jeon, and S.-Y. Heo, "Electrochemiluminescence Systems for the Detection of Biomarkers: Strategical and Technological Advances," *Biosensors (Basel)* 12, no. 9 (2022): 738, https://doi.org/10.3390/bios12090738.

32. V. A. Zamolo, G. Valenti, E. Venturelli, et al., "Highly Sensitive Electrochemiluminescent Nanobiosensor for the Detection of Palytoxin," *ACS Nano* 6, no. 9 (2012): 7989–7997, https://doi.org/10.1021/nn302573c.

33. Y. Zheng, H. Yang, L. Zhao, et al., "Lighting up Electrochemiluminescence-Inactive Dyes via Grafting Enabled by Intramolecular Resonance Energy Transfer," *Analytical Chemistry* 94, no. 7 (2022): 3296–3302, https://doi.org/10.1021/acs.analchem.1c05235.

34. X. Chen, Y. Liu, and Q. Ma, "Recent Advances in Quantum Dot-based Electrochemiluminescence Sensors," *Journal of Materials Chemistry C* 6, no. 5 (2018): 942–959, https://doi.org/10.1039/C7TC05474B.

35. J. Jiang, X. Lin, D. Ding, and G. Diao, "Graphitic-phase Carbon Nitride-based Electrochemiluminescence Sensing Analyses: Recent Advances and Perspectives," *RSC Advances* 8, no. 35 (2018): 19369–19380, https://doi.org/10.1039/C8RA02221F.

36. Y.-J. Li, W.-R. Cui, Q.-Q. Jiang, et al., "A General Design Approach toward Covalent Organic Frameworks for Highly Efficient Electrochemiluminescence," *Nature Communications* 12, no. 1 (2021): 4735, https://doi.org/10.1038/s41467-021-25013-8.

37. Y. Wang, G. Zhao, H. Chi, et al., "Self-Luminescent Lanthanide Metal-Organic Frameworks as Signal Probes in Electrochemiluminescence Immunoassay," *Journal of the American Chemical Society* 143, no. 1 (2021): 504–512, https://doi.org/10.1021/jacs.0c12449.

38. C. Alberoni, G. Pavan, T. Scattolin, and A. Aliprandi, "Critical Aspects and Challenges in the Design of Small Molecules for Electrochemiluminescence (ECL) Application," *Chempluschem* 89, no. 8 (2024): 202400142, https://doi.org/10.1002/cplu.202400142.

39. A. Zanut and F. Palomba, "Dye-Doped Silica Nanoparticles for Enhanced ECL-Based Immunoassay Analytical Performance," *Angewandte Chemie* 59, no. 49 (2020): 21858–21863, https://doi.org/10.1002/anie.202009544.

40. D. Pan, Z. Fang, E. Yang, et al., "Facile Preparation of WO3-x Dots with Remarkably Low Toxicity and Uncompromised Activity as Co-reactants for Clinical Diagnosis by Electrochemiluminescence," *Angewandte Chemie* 59, no. 38 (2020): 16747–16754, https://doi.org/10.1002/anie.202007451.

41. Y. Fang, H. Yang, Y. Hou, et al., "Timescale Correlation of Shallow Trap States Increases Electrochemiluminescence Efficiency in Carbon Nitrides," *Nature Communications* 15, no. 1 (2024): 3597, https://doi.org/10.1038/s41467-024-48011-y.

42. Z. Cao, C. Li, Y. Shu, et al., "Unraveling Mechanisms of Highly Efficient yet Stable Electrochemiluminescence from Quantum Dots," *Journal of the American Chemical Society* 145, no. 48 (2023): 26425–26434, https://doi.org/10.1021/jacs.3c10556.

43. K. Wu, R. Chen, Z. Zhou, et al., "Elucidating Electrocatalytic Oxygen Reduction Kinetics via Intermediates by Time-Dependent Electrochemiluminescence," *Angewandte Chemie* 62, no. 12 (2023): 202217078, https://doi.org/10.1002/anie.202217078.

44. Y. Wang, S. Zhou, Y. Zheng, et al., "Measurements of Local pH Gradients for Electrocatalysts in the Oxygen Evolution Reaction by Electrochemiluminescence," *Journal of the American Chemical Society* 147, no. 22 (2025): 19380–19390, https://doi.org/10.1021/jacs.5c04896.

45. H. Qi and C. Zhang, "Electrogenerated Chemiluminescence Biosensing," *Analytical Chemistry* 92, no. 1 (2020): 524–534, https://doi.org/10.1021/acs.analchem.9b03425.

46. C. Mwanza and S.-N. Ding, "Newly Developed Electrochemiluminescence Based on Bipolar Electrochemistry for Multiplex Biosensing Applications: A Consolidated Review," *Biosensors (Basel)* 13, no. 6 (2023): 666, https://doi.org/10.3390/bios13060666.

47. Y. Sun, S. Ge, R. Liu, et al., "Potential-resolved Electrochemiluminescence Biosensor for Simultaneous Determination of Multiplex miRNA," *Talanta* 266, no. Pt 2 (2024): 125063, https://doi.org/10.1016/j.talanta.2023.125063.

48. Y. Zhang, W. Liu, S. Ge, et al., "Multiplexed Sandwich Immunoassays Using Flow-injection Electrochemiluminescence with Designed Substrate Spatial-resolved Technique for Detection of Tumor Markers," *Biosensors & Bioelectronics* 41 (2013): 684–690, https://doi.org/10.1016/j.bios.2012.09.044.

49. X. Gao, X. Liu, Y. Zeng, Q. Zhang, B. Zhang, and G. Zou, "Spectrum-Resolved Electrochemiluminescence to Multiplex the Immunoassay and DNA Probe Assay," *Analytical Chemistry* 94, no. 45 (2022): 15801–15808, https://doi.org/10.1021/acs.analchem.2c03579.

50. X. Gou, Z. Xing, C. Ma, and J.-J. Zhu, "A Close Look at Mechanism, Application, and Opportunities of Electrochemiluminescence Microscopy," *Chemical & Biomedical Imaging* 1, no. 5 (2023): 414–433, https://doi.org/10.1021/cbmi.2c00007.

51. A. Zanut, A. Fiorani, S. Canola, et al., "Insights into the Mechanism of Coreactant Electrochemiluminescence Facilitating Enhanced Bioanalytical Performance," *Nature Communications* 11, no. 1 (2020): 2668, https://doi.org/10.1038/s41467-020-16476-2.

52. A. Fracassa, C. I. Santo, E. Kerr, et al., "Redox-mediated Electrochemiluminescence Enhancement for Bead-based Immunoassay," *Chemical Science* 15, no. 3 (2024): 1150–1158, https://doi.org/10.1039/D3SC06357G.

53. T. Smith, "The Hydrophilic Nature of a Clean Gold Surface," *Journal of Colloid and Interface Science* 75, no. 1 (1980): 51–55, https://doi.org/10.1016/0021-9797(80)90348-3.

54. J. Tkac and J. J. Davis, "An Optimised Electrode Pre-treatment for SAM Formation on Polycrystalline Gold," *Journal of Electroanalytical Chemistry* 621, no. 1 (2008): 117–120, https://doi.org/10.1016/j.jelechem.2008.04.010.

55. W. Miao, "Electrogenerated Chemiluminescence and Its Biorelated Applications," *Chemical Reviews* 108, no. 7 (2008): 2506–2553, https://doi.org/10.1021/cr068083a.

56. K. Sakanoue, A. Fiorani, C. I. Santo, et al., "Boron-Doped Diamond Electrode Outperforms the State-of-the-Art Electrochemiluminescence from Microbeads Immunoassay," *ACS Sensors* 7, no. 4 (2022): 1145–1155, https://doi.org/10.1021/acssensors.2c00156.

57. S. Rodríguez Muiña, G. Giagu, G. Valenti, and F. J. Del Campo, "Versatile Electrochemiluminescence Imaging Platform for Multiplexed Biosensing and Point-of-Care Application," *Chemical & Biomedical Imaging* (2026), https://doi.org/10.1021/cbmi.5c00274.

58. A. A. Yousif, N. S. Ahmed, and E. Mohamed, "An Overview of Biotin Interference Impact on Immunoassays," *Cyprus Journal of Medical Sciences* 10, no. 3 (2025): 162–168, https://doi.org/10.4274/cjms.2025.2024-71.

59. A. Fracassa, G. Ferrari, M. V. Balli, et al., "Stimuli-Responsive Luminophore Drives Mechanism Switch for Highly Efficient Electrochemiluminescence Immunosensing," *Journal of the American Chemical Society* 147 (2025): 35501–35509, https://doi.org/10.1021/jacs.5c10211.

60. C. I. Santo, G. Conejo-Cuevas, F. Paolucci, F. J. Del Campo, and G. Valenti, "Laser-Treated Screen-Printed Carbon Electrodes for Electrochemiluminescence Imaging," *Chem Biomed Imaging* 2, no. 12 (2024): 835–841, https://doi.org/10.1021/cbmi.4c00070.

Supporting Information

Additional supporting information can be found online in the Supporting Information section.

Supporting File: admi70560-sup-0001-SuppMat.docx.